

# An intelligent stand-alone ultrasonic device for monitoring local structural damage: implementation and preliminary experiments

Alexander Pertsch<sup>1,3</sup>, Jin-Yeon Kim<sup>1</sup>, Yang Wang<sup>1,4</sup> and Laurence J Jacobs<sup>1,2</sup>

<sup>1</sup> School of Civil and Environmental Engineering, Georgia Institute of Technology, Atlanta, Georgia 30332

<sup>2</sup> The George W. Woodruff School of Mechanical Engineering, Georgia Institute of Technology, Atlanta, Georgia 30332

E-Mail: yang.wang@ce.gatech.edu

**Abstract.** Continuous structural health monitoring has the potential to significantly improve the safety management of aged, in-service civil structures. In particular, monitoring of local damage growth at hot-spot areas can help to prevent disastrous structural failures. Although ultrasonic nondestructive evaluation (NDE) has proved to be effective in monitoring local damage growth, conventional equipment and devices are usually bulky and only suitable for scheduled human inspections. The objective of this research is to harness the latest developments in embedded hardware and wireless communication for developing a stand-alone, compact ultrasonic device. The device is oriented for the continuous structural health monitoring of civil structures. Relying on battery power, the device possesses functionalities of high-speed actuation, sensing, signal processing, and wireless communication. Integrated with contact ultrasonic transducers, the device can generate 1-MHz Rayleigh surface waves in a steel specimen and measure response waves. A Hilbert-transform-based envelope detection algorithm is presented for efficiently determining the peak values of the response signals, from which small surface cracks are successfully identified.

## 1. Introduction

Typically, the service life of a civil structure is at least on the order of several decades. During this period, the structural condition gradually deteriorates due to environmental influences, external loading, and natural hazards. For example, the National Bridge Inventory (NBI) in the U.S. lists over 600,000 bridges, 71,469 (or 12%) of which are classified as structurally deficient (US DOT 2009a). For bridges that are more than 40 years old (totaling about 300,000), the percentage of structurally deficient bridges reaches up to 20% (US DOT 2009b). These figures unequivocally demonstrate the need for regular inspections of bridges, which, due to limited resources, are commonly performed every 24 months. Current inspections are mainly visual, and are time- and labor-intensive. The inspections can only detect damage at the surface, yet internal

---

<sup>3</sup> Present address: Institute for System Dynamics, University of Stuttgart, Pfaffenwaldring 9, 70569 Stuttgart, Germany

<sup>4</sup> Author to whom any correspondence shall be addressed to.

damage may remain unnoticed. In addition, the results obtained from visual inspections are highly subjective, and the classification of the same bridge can vary significantly among different inspectors (Moore *et al.* 2001).

To obtain reliable and objective evaluations of the structural condition, various structural health monitoring (SHM) techniques have been proposed (Sohn *et al.* 2001, Elgamal *et al.* 2003, Chang *et al.* 2003). A SHM system contains sensors and data acquisition modules that measure structural response, as well as data analysis modules for interpreting structural conditions. As a common approach in SHM, modal analysis is usually conducted upon vibration data; changes in the modal behavior are used to assess the structural condition. However, such approaches focusing on global modal characteristics are usually insensitive to local defects, and will likely miss the critical growth of local damage. Thus, global SHM approaches need to be supplemented with local approaches to improve the sensitivity for damage detection.

A recent trend in SHM systems is the exploration of wireless communication technologies. Traditional cable-based SHM systems require running long cables all over the structure, which can be expensive in terms of both installation time and monetary costs. Investigations show that the installation of such a tethered SHM system typically takes up to 75% of the total testing time (Straser and Kiremidjian 1998). The cost of one sensing channel installed in a typical low-rise building is approximately \$1,000 for hardware and an additional \$2,000 for the installation (Çelebi 2002). To eliminate the high cost associated with cabling, Straser and Kiremidjian (1998) demonstrated the feasibility and cost-effectiveness of a wireless SHM system. Later on, Wang *et al.* (2007) developed a prototype wireless sensing system, which consists of multiple compact, self-contained data-acquisition and processing devices that operate on batteries and communicate over a wireless connection. Through field tests, the performance of the system was demonstrated to be comparable to the performance of a commercial tethered system (Lynch *et al.* 2006; Wang *et al.* 2006). Furthermore, a flurry of research in wireless SHM has been reported in recent years (e.g. Nagayama and Spencer 2007, Kim *et al.* 2007; Weng *et al.* 2008). Nevertheless, previous studies on wireless SHM largely focused on global modal characteristics extracted from structural vibration data. Thus, most techniques are not applicable for the continuous monitoring of small and local damage growth.

As a well-known technique for detecting small local-level defects, ultrasonic nondestructive evaluation (NDE) is well established and has long been used for local damage evaluation, such as cracks and corrosion (Tien *et al.* 1981, Resch and Nelson 1992, Meyendorf *et al.* 2004). However, most of current ultrasonic NDE techniques require a trained inspector and bulky commercial ultrasonic equipment operating on AC power. Due to the size, weight, and cost, such equipment is generally not suitable for continuous monitoring in the field. On the other hand, due to the high labor costs, shortening the sparse biennial inspection interval is not an option. Therefore, traditional NDE technologies cannot provide a solution for the continuous monitoring of critical crack growth, which can be severe during the two-year inspection interval.

This study explores the latest digital signal processing hardware and wireless communication technologies for the development of a compact wireless ultrasonic device that is suitable for the continuous monitoring of local damage growth. Compared with previous wireless SHM studies that focus upon modal analysis, the challenges of developing such a wireless ultrasonic device are mainly twofold. First, the vibration signals obtained for global modal analysis typically have frequency components less than a few hundred Hz, for which a sampling rate on the order of 100 Hz to some kHz is sufficient. Ultrasonic signals, however, are usually signals with frequencies above hundreds of kHz and need sampling rates on the order of several MHz, which cannot be provided by previous wireless SHM platforms. Second, most SHM systems only require passive sensing, i.e. no actuation signal needs to be generated by the wireless device. In contrast, ultrasonic testing is an active technique, which requires the generation of sufficiently strong ultrasonic excitation in the appropriate frequency range. A stronger actuation signal yields a stronger response signal and a higher signal-to-noise ratio (SNR). However, when a compact and stand-alone device has to limit its power supply to batteries, a compromise between signal quality and power requirements must be achieved.

Lynch (2005) investigates the concept of wireless active sensing by integrating a 32-bit Motorola PowerPC MPC555 microcontroller with sensing and actuation interfaces. For a piece of thin aluminum plate, Lamb waves are generated and measured through two separate lead-zirconate-titanate (PZT) piezoelectric pads; both actuation and sensing interfaces operate at a sampling rate of 40 kHz. In Liu and Yuan's (2008) work, an external HP 33120A function generator and a KH-7602 power amplifier are used to launch 40~90 kHz Lamb waves through piezoelectric discs into an aluminum plate; a field-programmable gate array (FPGA) chip is adopted to achieve sampling frequencies at a few MHz. In addition to such studies using pitch-catch wave propagations for crack/notch detection, other studies in wireless active sensing investigate impedance-based techniques that consume less battery power. The electro-mechanical impedance of a piezoelectric patch attached to a structure is usually measured around tens of kHz range, and typical applications have been the detection of bolt loosening (Grisso 2005, Park *et al.* 2006, Mascarenas *et al.* 2007).

In contrast, the wireless ultrasonic device developed in this study is built around a sophisticated digital signal processor (DSP). The general concept for the prototype device is introduced by Pertsch *et al.* (2009). Adhering to the power limit imposed by ordinary batteries, the stand-alone device can generate Rayleigh waves (centered around 1 MHz) into a thick piece of metal specimen through contact ultrasonic transducers, as well as detect the response ultrasonic wave at a sampling rate of 8.3334 MHz. An efficient envelope detection algorithm based on the Hilbert transform is presented, and the envelope amplitude is adopted as a damage signature. To validate the performance of the prototype device, experiments are conducted with a steel specimen manufactured with small notches of various depths (0.5 mm ~ 3.2mm) imitating crack initiation. Measurement results obtained with the prototype device are shown to be comparable to

measurements with commercial ultrasonic NDE equipment, and various surface notches are successfully detected by the wireless device.

Overall, the prototype device aims to combine the advantages of traditional SHM and NDE systems. Compared with traditional SHM systems, the prototype device offers the favorable local resolution enabled by ultrasonic evaluation, allowing for the continuous monitoring of local damage growth at hot-spot areas. On the other hand, compared with traditional NDE systems, the prototype device has much smaller size and lower cost; it is suitable for permanent deployment on a structure without the need for lengthy cables or AC power. Section 2 of this paper describes the hardware layout and functional components of the prototype device; Section 3 presents the envelope detection algorithm based on the Hilbert transform; Section 4 describes the laboratory validation experiments and results; Section 5 provides a summary and discussion of the work.

## **2. General concept and hardware layout of the device**

The main functionality of the ultrasonic monitoring device can be described as the following four tasks: 1) *wireless communication*, 2) *actuation signal generation*, 3) *response signal detection*, and 4) *signal processing*. Figure 1 shows the functional components of the prototype device. At the beginning of an ultrasonic test, the microprocessor initializes its memory and peripherals, and waits for the start command from the server. To initiate a test, a wireless start command is sent from the server (i.e. a computer connected with a wireless transceiver) to the prototype device. Upon receiving the start command through the wireless transceiver, the microprocessor activates the signal generation module, and transmits a pulse-width modulation (PWM) signal to the output amplification board. The output amplification board then amplifies the signal amplitude to  $\pm 18$  V, and shifts the mean voltage to be around 0 V. The amplified signal is injected into the transmitting ultrasonic transducer, which generates the ultrasonic wave in the underlying specimen. After traveling in the specimen, the wave is detected by the receiving ultrasonic transducer. Through a signal conditioning board, the detected signal is conditioned to be ready for analog-to-digital conversion by the microprocessor. The microprocessor may process the data, and send the data or results wirelessly back to the server. This section first introduces the individual hardware components, and then describes the signal generation task, the signal detection task, and the communication task. Details on the signal processing task will be provided in Section 3.

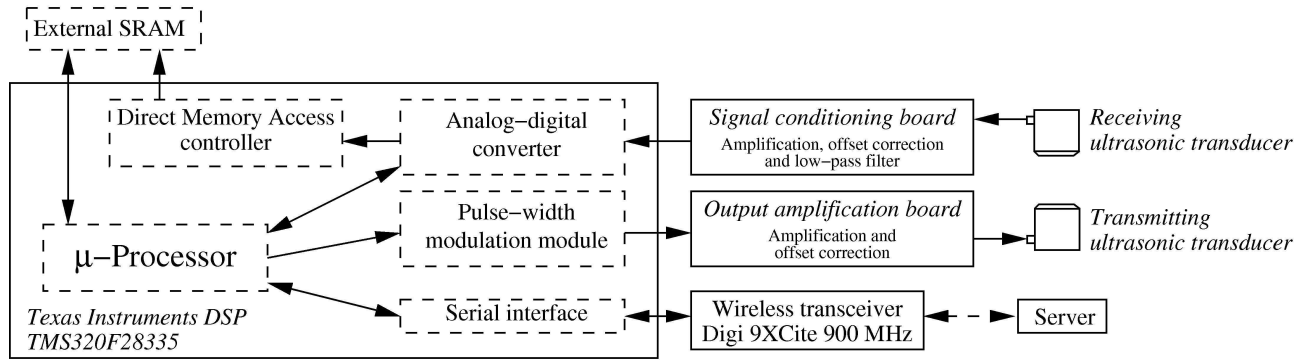


Figure 1. Functional modules of the prototype device.

### 2.1 Hardware components

The prototype device is built upon a *Texas Instruments eZdsp<sup>TM</sup> F28335* evaluation board, which offers a convenient interface for software implementation on a *Texas Instruments TMS320F28335* digital signal processor (DSP) operating at 150 MHz. Among other features, this DSP chip contains a floating-point unit (FPU, used for signal processing), an analog-digital converter (used for signal detection), a pulse-width modulation module (used to generate ultrasonic signals) and a serial interface to which a commercial *Digi 9XCite* wireless transceiver is connected. The DSP provides  $256\text{K} \times 16$  bits non-volatile internal flash memory for program code, and  $34\text{K} \times 16$  bits internal volatile single access random access memory (SARAM) for embedded computing. The *eZdsp<sup>TM</sup> F28335* evaluation board provides an additional external SRAM chip of  $128\text{K} \times 16$  bits, which can also be used for embedded computing.

Figure 2(a) shows the *eZdsp<sup>TM</sup> F28335* evaluation board. The two flat ribbon cables, one for analog signals and one for digital signals, are connected to pin-header sockets at the bottom side of the connector board (figure 2(b)). As an extension of the evaluation board, the connector board in figure 2(b) provides BNC connectors for both generating output signals and receiving response signals, as well as a socket for plugging in the *Digi 9XCite* wireless transceiver. Standard  $50\ \Omega$  coaxial cables are used to route the output PWM signal of the connector board into the output amplification board (figure 2(d)), and from there on to the transmitting ultrasonic transducer. On the other hand, response signals from the receiving ultrasonic transducer are routed to the signal conditioning board (figure 2(c)), and from there back to the analog-to-digital conversion (ADC) input on the connector board. In the prototype device, the circuits have been implemented on separate boards, so that they can be developed and tested independently from each other, and an individual board can easily be replaced. It should be noted that the current prototype design has focused upon the functionality, and has not been optimized for compactness. For example, many peripherals on the *eZdsp<sup>TM</sup> F28335* evaluation board are general-purpose components that are not needed for this application.

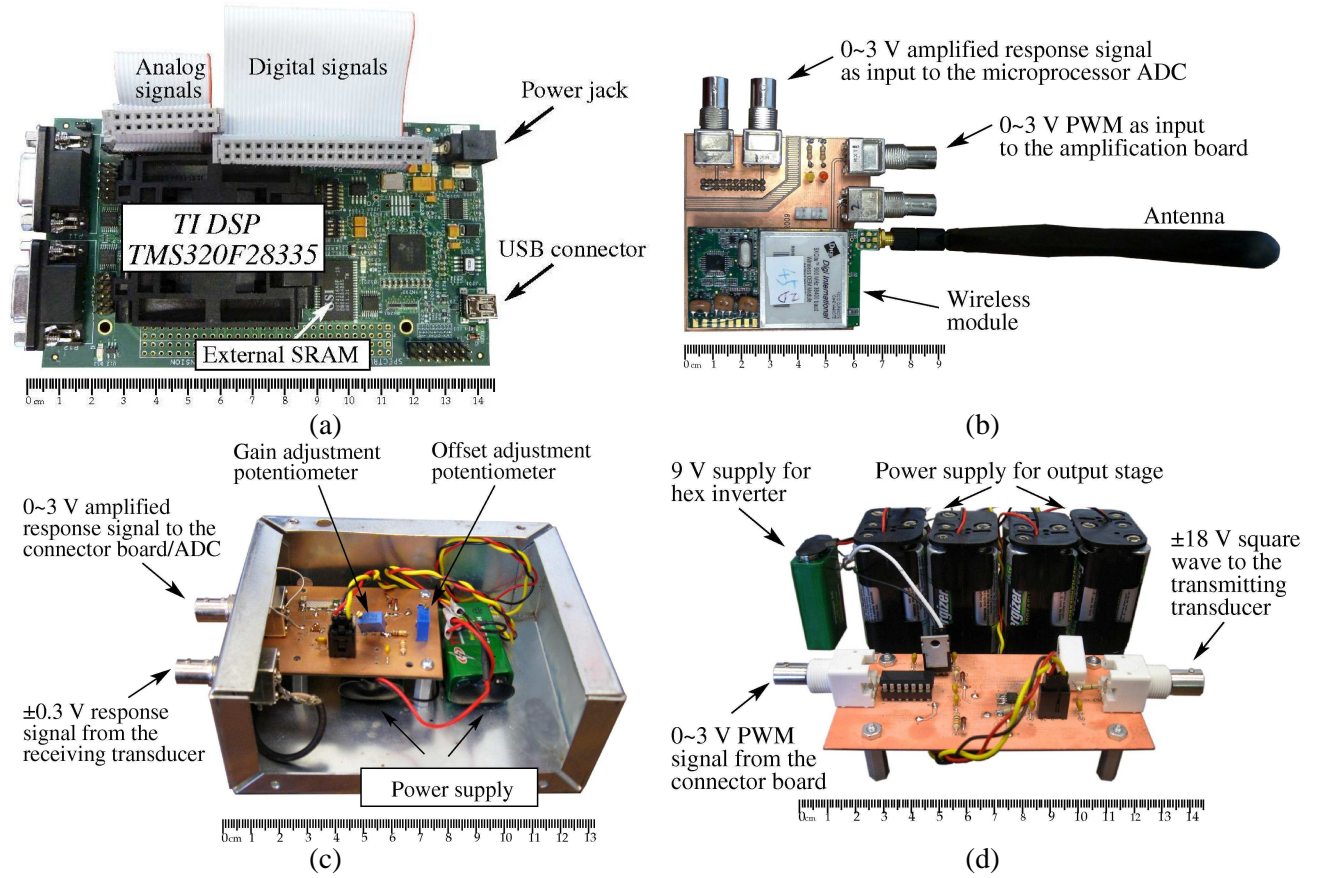


Figure 2. Photos of the hardware components: (a) eZdsp™ F28335 evaluation board; (b) Connector board with wireless transceiver; (c) Signal conditioning board; (d) Output amplification board.

## 2.2 Signal generation

The signal generation task involves the PWM module of the *TMS320F28335* microprocessor, as well as the output amplification board (figure 2(d)). The module generates a 0 ~ 3 V tone burst PWM signal, which is amplified and shifted to a  $\pm 18$  V square wave by the output amplification board. The amplified signal is then fed into the transmitting ultrasonic transducer.

### 2.2.1 Signal generation using PWM

The PWM module of the *TMS320F28335* microprocessor can generate a square wave, which alternates between a high level (3 V) and a low level (0 V). The ratio of the high-level duration to the low-level duration during one period determines the duty cycle. As the signal source for ultrasonic excitation, the PWM module generates a short tone burst, which consists of multiple periods of a 50%-duty-cycle square wave. Since the selected ultrasonic transducers operate around 1 MHz, the frequency of the PWM signal is also set to 1 MHz. The length of the burst, i.e. the number of periods, is configurable. To provide excitation that is strong enough, the 0 ~ 3 V PWM signal is boosted to a  $\pm 18$  V square wave by the output amplification board, and shifted to zero mean value. The amplified square wave is then fed into the transmitting ultrasonic

transducer. Since the transmitting transducer acts as a narrowband bandpass filter and only passes signals around 1 MHz, the ultrasonic wave generated by the transducer becomes a sinusoidal mechanical wave burst.

The Fourier series of a  $\pm 18\text{V}$  1-MHz square wave with 50%-duty-cycle can be examined to verify the effectiveness of this electrical-mechanical filtering:

$$\hat{s}(t) = \frac{72}{\pi} \sum_{k=1,3,\dots}^{\infty} \frac{\sin(2\pi k f_0 t)}{k} \quad (1)$$

where  $f_0$  is the base frequency of 1 MHz. The equation shows that the 1 MHz sinusoidal component of the square wave oscillates at an amplitude of  $72/\pi \approx 22.9\text{ V}$ . In addition, the amplitude of the 2<sup>nd</sup> major frequency component (3 MHz) is about 7.96 V, the 3<sup>rd</sup> major frequency component (5 MHz) is about 4.77 V, etc. As a result, the 1 MHz signal can be sufficiently passed by the transducer, while all other higher-frequency components can be effectively suppressed by a properly selected transducer with a narrow passband around 1 MHz.

### 2.2.2 Output amplification

The output amplification circuit is intended to boost the excitation signal to a level of approximately  $\pm 18\text{ V}$ . To this end, a circuit presented by Johnson and Associates (2000) is adapted to provide the desired power levels and work with the capacitive load of a piezoelectric transducer. A schematic of the implemented output amplification circuit is shown in figure 3.

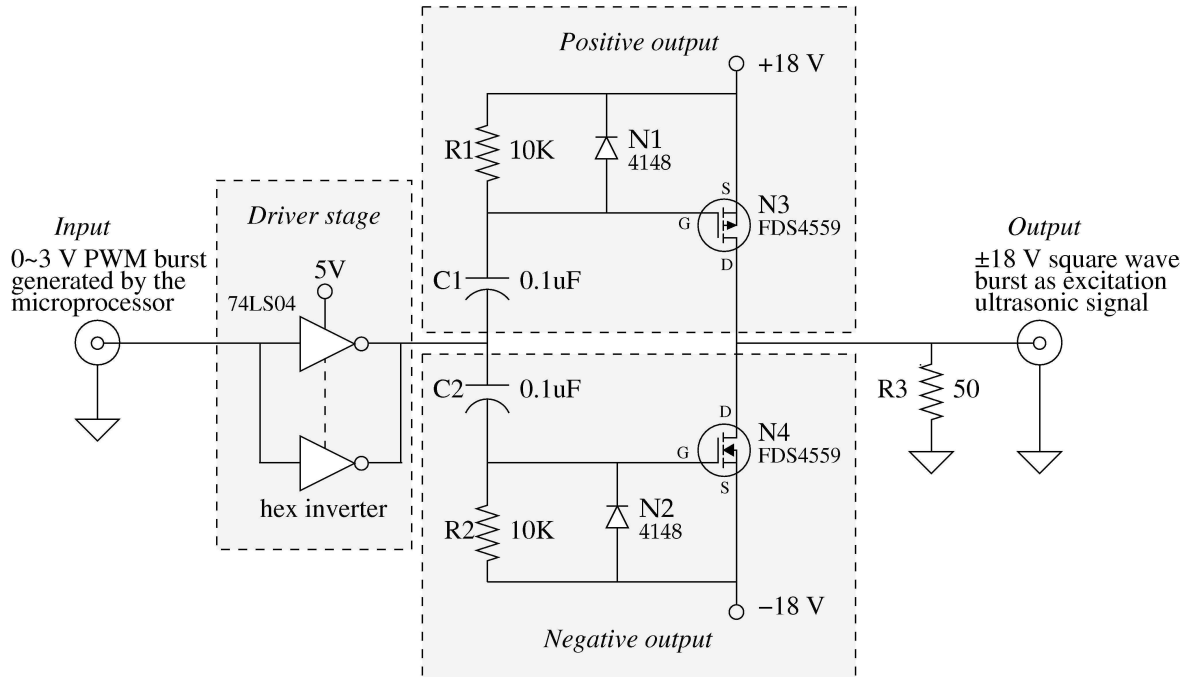


Figure 3. Schematic of the output amplification circuit.

In this circuit, a *74LS04* hex inverter in the driver stage first inverts and amplifies the 0 ~ 3 V input signal to a 0 ~ 5 V level, so that the output of the hex inverter can drive the metal-oxide semiconductor field effect transistors (MOSFETs) *FDS4559*. A MOSFET controls the current flow from source (S) to drain (D) with the voltage applied at the gate (G). The circuit is designed symmetrically, with the upper half intended to be active for providing the positive (+18 V) half-cycle, and the lower half providing the negative (−18 V) half-cycle. The two halves only differ by the type of MOSFET transistors used: a p-channel enhancement mode *FDS4559* transistor in the upper half, and an n-channel enhancement mode *FDS4559* transistor in the lower half. Capacitors on the order of 0.1  $\mu$ F are connected between signal line and ground to dampen noise and voltage ripples. The amplified wave burst signal is fed into the transmitting ultrasonic transducer, which, as a piezoelectric device, is predominantly a capacitive load. The equivalent capacitor charges and discharges slowly in the presence of a (stray) DC offset in the signal, which can cause distortions in the mechanical wave burst. To avoid such distortion, the resistor  $R_3$  provides a path to the ground for the DC current, enabling a faster response of the transducer; note that the resistance of  $R_3$  matches the nominal impedance of the transducer. In stand-by mode, as long as no alternating current enters the input of the amplification circuit, both MOSFETs  $N_3$  and  $N_4$  inhibit current flow; thus, no current can flow through resistor  $R_3$  and negligible energy is dissipated.

### 2.2.3 Performance of the signal generation module

To measure the ultrasonic wave generated by the transmitting ultrasonic transducer, a second transducer is directly clamped face-to-face with the transmitting transducer. When the transmitting transducer is excited by the square wave burst generated by the output amplification circuit, the response voltage of the second transducer is measured directly with an oscilloscope. Figure 4 shows the five cycles of 1-MHz 0~3V PWM signal generated by the microprocessor, as well as the response signal of the second transducer. The electrical-mechanical filtering mechanism is shown to successfully generate a tone burst signal centered around 1-MHz at the second transducer, with a peak voltage as high as 3 V. After the excitation starts, the mechanical oscillation of the piezoelectric transducer needs time to build up. Due to the low mechanical damping, the response signal does not end abruptly after the PWM signal ends, but dampens out slowly.



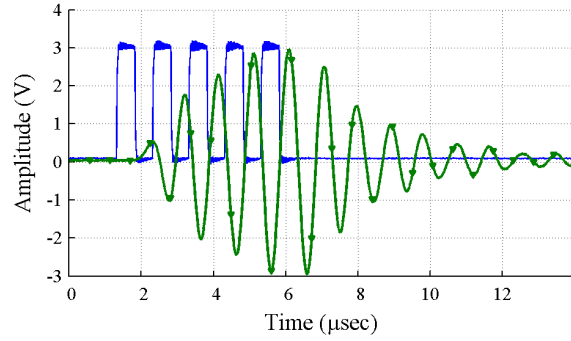


Figure 4. Comparison of the PWM (0 ~ 3V) signal (—) with the resulting mechanical wave form (—▼—). The mechanical wave form is measured using a second transducer clamped face-to-face to the transmitting transducer.

### 2.3 Signal detection

To use the wireless ultrasonic device in a pitch-catch setup, the transmitted ultrasonic wave excites the testing specimen first. The wave travels through and scatters in the specimen, and then is captured by the receiving ultrasonic transducer. The output voltage of the receiving transducer is usually low-amplitude and noisy (particularly when compared to the response of a face-clamped transducer shown in figure 4). Prior to analog-to-digital conversion (ADC), the signal needs to be amplified and shifted by the specially designed signal conditioning circuit shown in figure 2(c).

#### 2.3.1 Analog-to-digital conversion

The TMS320F28335 microprocessor contains a 12-bit ADC module with an input range of 0 ~ 3 V, which results in an ideal quantization error of 0.733 mV. Using the Direct Memory Access (DMA) controller of the TMS320F28335, sampled data is directly transferred from the ADC output registers into the external SRAM, bypassing the CPU. Not involving the CPU in the data transfer enables fast and reliable data transfers that are not affected by other concurrent workload of the CPU. With the microprocessor running at a 150-MHz clock, reliable sampling is possible with a sampling rate of 8.3334 MHz, which provides a Nyquist frequency of 4.1667 MHz. Therefore, the sampling rate is sufficient for acquiring ultrasonic signals centered around 1 MHz.

#### 2.3.2 Signal conditioning

With an 18 V excitation signal fed into the transmitting transducer, the output voltage of the receiving transducer usually has an amplitude of about 0.3 V, with a mean value of 0 V. To increase the signal-to-noise ratio (SNR), as well as to reduce the effect from quantization error, the output signal of the receiving transducer is amplified and shifted so that it better occupies the entire ADC input range of 0 ~ 3 V. To avoid aliasing effects in the sampled signal, the highest frequency component in the signal should be lower than the Nyquist frequency of 4.1667 MHz.

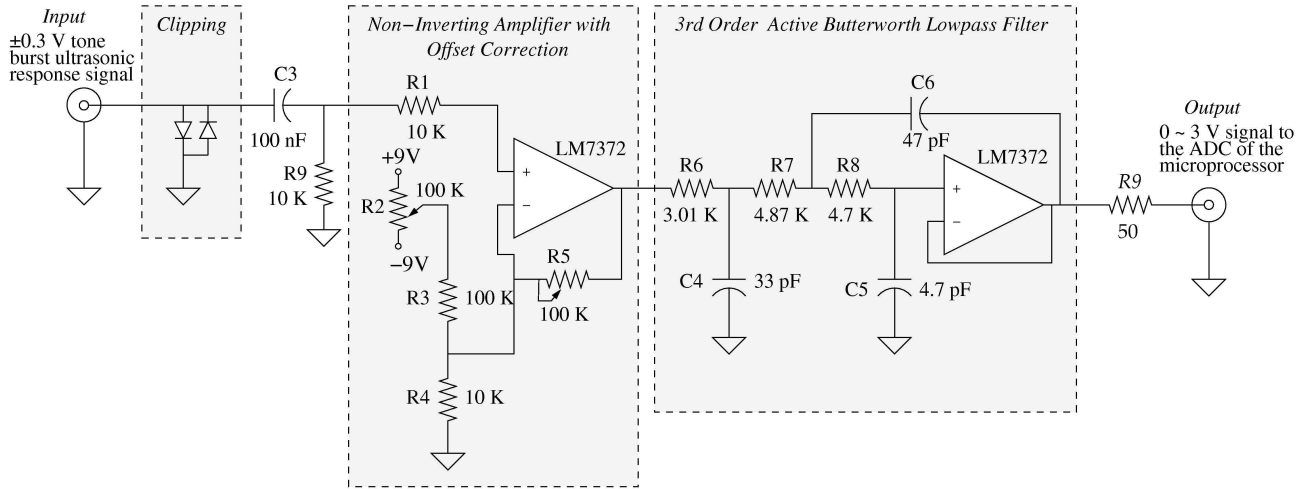


Figure 5. Schematic of the signal conditioning circuit

Figure 5 shows the schematic of the signal conditioning circuit. The two diodes at the left of the schematic clip the amplitude of the incoming voltage signals to a maximum voltage that corresponds to the forward voltage drop of a diode (0.6 ~ 0.7 V). This protects the rest of the circuit and the analog-digital converter from harmful peak surge voltages, which, for example, can occur when the transducer is accidentally bumped against a hard surface. The capacitor  $C_3$  and the resistor  $R_9$  form a high-pass filter that blocks the DC offsets. The cutoff frequency of 159 Hz of this high-pass filter is sufficiently high to block any low frequency distortions or offsets, as well as sufficiently low for passing the ultrasonic signal centered around 1 MHz.

The next stage of the circuit is a non-inverting amplifier with variable amplification gain and offset adjustment. Let  $\alpha \in [0,1]$  describe the wiper position of the potentiometer  $R_2$ , with  $\alpha = 0$  representing the voltage at the wiper is equal to  $-9$  V and  $\alpha = 1$  representing the voltage at the wiper is  $+9$  V. Furthermore, let  $\beta \in [0,1]$  describe the wiper position of the potentiometer  $R_5$ , where  $\beta = 0$  represents the case when the potentiometer is shorted (with zero resistance), and  $\beta = 1$  represents the case when the potentiometer resistance is 100 k $\Omega$ . The following relation between the output and the input of the non-inverting amplifier can be obtained through circuit analysis:

$$V_{\text{out}} = \underbrace{-\frac{(2\alpha-1)\beta R_5}{(1-\alpha)\alpha R_2 + R_3} 9V}_{\text{Offset}} + \underbrace{\left[ \frac{\beta R_5}{(1-\alpha)\alpha R_2 + R_3} + \frac{\beta R_5}{R_4} + 1 \right]}_{\text{Gain}} V_{\text{in}} \quad (2)$$

With current components, the amplification circuit can provide a maximum voltage gain of 12 or 21.6 dB, and a maximum adjustable offset of  $\beta \cdot (\pm 9$  V). The *National Semiconductor LM7372* op-amp in use offers a gain-bandwidth product of 100 MHz and a slew rate of 700 V/ $\mu$ s when driven by  $\pm 5$  V. Thus, the *LM7372* offers a sufficiently high gain and a sufficiently fast response for the desired 1 MHz tone burst signal.

The next stage in figure 5 is a 3<sup>rd</sup>-order active Butterworth low-pass filter with a cutoff frequency of 2.5 MHz, so that signals with frequencies over the Nyquist frequency (4.1667 MHz) can be effectively eliminated. The Butterworth filter features a maximum flat passband response, at the expense of steepness in the transition region from passband to stopband, and also at the expense of a poorer phase characteristic. Other filter designs, e.g. Bessel filter, may offer more linear phase performance, but provide a poorer amplitude characteristic (Horowitz and Will 1989). As the amplitude of the received signal is adopted as a damage signature in this study, the advantage of a Butterworth filter in terms of flat passband response surpasses its disadvantages. Finally, due to the negative feedback loop in the Butterworth filter, the output impedance of the amplification circuit is nearly zero, which leads to an impedance mismatch with the 50  $\Omega$  coaxial cable that connects the amplification board to the ADC. To prevent energy reflection due to this impedance mismatch, the resistor  $R_9$  increases the output impedance of the signal conditioning circuit to 50  $\Omega$ .

### 2.3.3 Performance of the signal detection module

To assess the performance the signal conditioning circuit combined with the microprocessor ADC, a 1-MHz sinusoidal wave with 0.3 V amplitude, generated by an *Agilent 33250A* function generator, is fed as the input to the signal conditioning circuit. To achieve the necessary amplification and mean shifting,  $\alpha$  is set to be around 0.23 and  $\beta$  around 0.37. The output of the circuit is then sampled by the ADC of the *TMS320F28335* microprocessor and shown in figure 6. The frequency spectrum has a dominant peak at the original 1-MHz frequency; distortions at other frequencies are negligible compared to the dominant frequency.

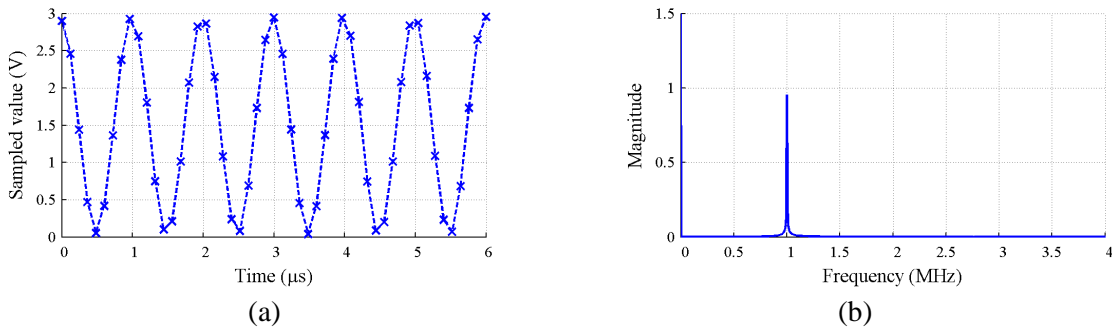


Figure 6. Microprocessor ADC sampling results of the signal conditioning output; input to the signal conditioning circuit is an 1-MHz sinusoidal input with 0.3 V amplitude; (a) ADC samples: y-axis corresponds to the full measurement range of the ADC (0 ~ 3 V); (b) FFT magnitude of the sampled signal.

## 2.4 Communication

The *Digi 9XCite* transceiver is used for wireless communication between the device and a server. With a 2.1 dBi dipole antenna, the transceiver provides communication with a continuous data stream of up to 38400 bps, over a distance of up to 90 m indoor or up to 300 m outdoor. This communication range is

usually sufficient for typical field applications with short- or mid-span bridges. Operating in the 902–928 MHz ISM (industrial, scientific and medical) radio band with a transmit power of 4 mW, the wireless device can operate in North America, Australia, South Korea, Israel, etc., without the need for an individual license. Compared to 2.4 GHz devices, which can be used worldwide, 900 MHz devices typically offer longer communication range given the same amount of power consumption (Digi International Inc. 2010). Communication between the wireless module and the microprocessor uses the UART (universal asynchronous receiver/transmitter) interface. Enabled by pin-to-pin compatibility, when necessary, the *9XCite* transceiver in the prototype device can also be easily replaced by a *Digi 24XStream* transceiver that operates at the 2.4 GHz band. The wireless module groups data into packets of up to 64 bytes. Cyclic redundancy check (Press *et al.* 1992) is adopted for detecting erroneous transmissions. If the checksum is incorrect, the packet is dropped. The *9XCite* does not automatically retransmit if a packet is dropped, therefore, the application has to ensure that data is successfully received.

### 3. Data processing

When the transmitting transducer generates a tone burst signal, the response signal measured at the receiving transducer may consist of one or more tone bursts. To identify these bursts, the envelope of the measured signals is determined through the Hilbert transform (Lyons 2004, Sec. 9.2). Peak amplitude values of the envelopes can be used as quantitative measures for damage assessment. Using the envelope of the sampled signal, the peak amplitude can be obtained with higher accuracy than directly taking the maximum absolute value among the data samples, as the samples may easily miss the peak of the original signal. To avoid wireless transmission of lengthy time histories, the *IEEE-754* single-precision (32 bit) floating-point unit (FPU) of the *TMS320F28335* microprocessor is utilized for efficient on-board data processing. After on-board processing, only the envelope results (instead of lengthy time histories) need to be transmitted back to the server, which helps save time and battery power needed by the wireless transmission. The reduction in transmission payload also allows more devices to operate on the same channel.

#### 3.1 Envelope detection using Hilbert transform in continuous time

Although the sampling frequency of the device ( $f_s = 8.3334$  MHz) is sufficient in this application, it is not significantly higher than the 1-MHz dominant frequency of the response signal. Therefore, the original peak values of the tone burst can be easily missed by the samples. The discrete Hilbert transform is chosen to calculate the envelope signal, whose maximum amplitude offers a close approximation to the original peak value of the tone burst. To illustrate the principle of envelope detection through Hilbert transform, first consider a continuous time signal  $u(t)$ . Using the Cauchy principal value (CPV), the Hilbert transform of  $u(t)$  is obtained as another time-domain signal (Hahn 1996):

$$\mathcal{H}\{u(t)\} = -\frac{1}{\pi} \text{CPV} \int_{-\infty}^{\infty} \frac{u(\eta)}{\eta - t} d\eta \quad (3)$$

Using the Hilbert pair,  $u(t)$  and  $\mathcal{H}\{u(t)\}$ , a complex analytic function can be composed:

$$s(t) = u(t) + i \cdot \mathcal{H}\{u(t)\} \quad (4)$$

where  $i$  is the imaginary unit. It is known that the Fourier transforms of  $u(t)$  and  $s(t)$  are related as (Hahn 1996):

$$\mathcal{F}\{s(t)\} = (1 + \text{sgn}(\omega)) \mathcal{F}\{u(t)\} \quad (5)$$

where  $\text{sgn}(\cdot)$  is the sign function. Therefore,  $\mathcal{F}\{s(t)\}$  can be easily calculated based upon  $\mathcal{F}\{u(t)\}$ ; then  $s(t)$  can be determined by inverse Fourier transform. Note that the Fourier transform of  $s(t)$  vanishes for negative frequencies.

The measured tone burst signal can be described as an amplitude modulated signal with carrier wave  $\cos(\omega_0 t + \varphi)$  and time-varying amplitude or envelope signal  $e(t) \geq 0$ :

$$u(t) = e(t) \cos(\omega_0 t + \varphi) \quad (6)$$

where the carrier frequency  $\omega_0$  corresponds to the dominant carrier frequency of the ultrasonic signal and  $\varphi$  represents the phase angle. As described in Section 2.2.1, the carrier frequency  $\omega_0$  is chosen as  $2\pi \cdot 1$  MHz in this study. The receiving transducer, which measures the amplitude-modulated tone burst signal, acts as a narrowband band-pass filter. As a result, the frequency content of the envelope signal  $e(t)$  is distinctly lower than the carrier frequency. According to Bedrosian's theorem (Bedrosian 1976), the Hilbert transform of their product can be obtained by taking the Hilbert transform of the higher-frequency signal and multiplying it with the lower-frequency time-domain signal:

$$\mathcal{H}\{u(t)\} = e(t) \mathcal{H}\{\cos(\omega_0 t + \varphi)\} = e(t) \sin(\omega_0 t + \varphi) \quad (7)$$

Substituting Eqs. (6) and (7) into Eq. (4), the complex analytic function that corresponds to  $u(t)$  is:

$$s(t) = e(t) [\cos(\omega_0 t + \varphi) + i \cdot \sin(\omega_0 t + \varphi)] \quad (8)$$

Taking the absolute value of the equation above, it is clear that  $e(t) = |s(t)|$ . In summary, the following procedures can be followed for calculating the envelope signal:

1. Obtain the Fourier transform of the response signal  $u(t)$ ;
2. Calculate the Fourier transform of the analytic signal as  $\mathcal{F}\{s(t)\} = (1 + \text{sgn}(\omega)) \mathcal{F}\{u(t)\}$ ;
3. Take the inverse Fourier transform to find  $s(t)$ ;

4. Obtain the envelope signal as  $e(t) = |s(t)|$ .

### 3.2 Numerical implementation in discrete time

In the numerical implementation, the device processes discrete-time signals instead of continuous-time signals. For clarity, refer to the discrete-time signals as “sequences.” Given a discrete-time sequence  $u[n]$ ,  $n = 0, 1, \dots, N-1$  (for efficient calculations we assume  $N$  to be a power of 2), the discrete-time Fourier transform (DFT)  $U[k]$  can be computed through the fast Fourier transform (FFT) (Press *et al.* 1992). Sequences inherently can not be “analytic” as this property refers to continuous-time functions. However, an “analytic-like” sequence can be defined whose DFT is zero for negative frequencies. Following the approach suggested by Marple (1999), the discrete Fourier transform of the analytic-like sequence  $s[n]$  is given as:

$$S[k] = \begin{cases} U[0] & \text{for } k = 0 \\ 2U[k] & \text{for } 1 \leq k \leq \frac{N}{2} - 1 \\ U[\frac{N}{2}] & \text{for } k = \frac{N}{2} \\ 0 & \text{for } \frac{N}{2} + 1 \leq k \leq N - 1 \end{cases} \quad (9)$$

The equation uses a common notation for the DFT, where  $S[k]$ ,  $k = 0 \dots \frac{N}{2}$  corresponds to positive frequencies with  $S[\frac{N}{2}]$  being the frequency content at the Nyquist frequency;  $S[k]$ ,  $k = \frac{N}{2} + 1 \dots N - 1$  corresponds to negative frequencies. In Eq. (9), the constant coefficients in front of  $U[k]$  (such as 0, 1, and 2) are mostly determined by the relationship described in Eq. (5). Note that  $U[\frac{N}{2}]$  is not multiplied by 2, which is to ensure that the real part of the “analytic-like” sequence  $s[n]$  is identical to the original sequence  $u[n]$  (as required by Eq. (4)). After the calculation described in Eq. (9), the discrete-time sequence  $s[n]$  is then obtained by applying the inverse FFT to  $S[k]$ , and finally, the absolute values of  $s[n]$  provide the envelope sequence  $e[n]$ .

As an example, figure 7(a) shows a modulated signal with carrier frequency  $f_0 = 1$  MHz:

$$f(t) = e^{-\gamma(t-t_d)^2} \sin(2\pi f_0 t) \quad (10)$$

where the modulation constants include the decay coefficient  $\gamma = 3 \times 10^{11}$  and the time delay  $t_d = 5$  ms. Figure 7 shows the signal and its frequency spectrum centered around 1 MHz. As indicated by the cross markers in figure 7(a), the signal is sampled at  $f_{s,\text{example}} = 3.125$  MHz (which is well below the ADC sampling rate of the wireless device), to make the envelope detection more challenging. The sampled data is then fed into the algorithm described above, so that the envelope curve (dashed line) is detected through the Hilbert transform. As the original signal only has negligible frequency content at or above the Nyquist frequency  $f_{s,\text{example}}/2 \approx 1.56$  MHz (as shown in figure 7(b)), the sampled sequence contains all necessary information for reconstructing the original signal. In particular, despite the relatively low sampling frequency, envelope

detection using the Hilbert transform yields a good estimation of the envelope curve of the original signal, and hence for the peak amplitude of the original signal.

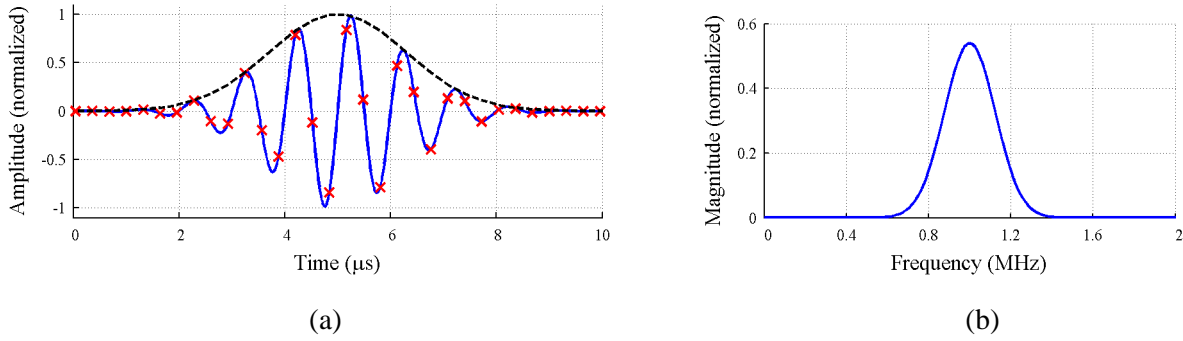


Figure 7. Envelope detection through the Hilbert transform of data sampled at  $f_s = 3.125$  MHz: (a) Time domain signal, — original signal,  $\times$  sampled sequence, -- envelope curve of sampled sequence; (b) Frequency spectrum of the signal.

### 3.3 Burst detection and data reduction

Upon a tone burst excitation by the transmitting transducer, the response measured at the receiving transducer usually consists of one or more bursts. Besides improving the accuracy for estimating the peak amplitude, the envelope signal is also used to identify these bursts and distinguish them from noise. Figure 8 shows an example of a measured signal, which has been directly obtained as the output of the ADC. The envelope detection procedures are applied directly to the signal, without any prior digital filtering. As illustrated in figure 8, the envelope signal is compared to a pre-defined threshold. A tone burst is assumed to last from the first time the envelope signal exceeds this threshold until the envelope drops below the threshold. The threshold is chosen manually during the first installation of the system on a structure, based on sample measurements and taking into account the signal strength, the noise level, and other disturbances in the measurements. It should be chosen sufficiently high so that no noise is falsely identified as a signal burst, and also sufficiently low so that no signal burst is omitted.

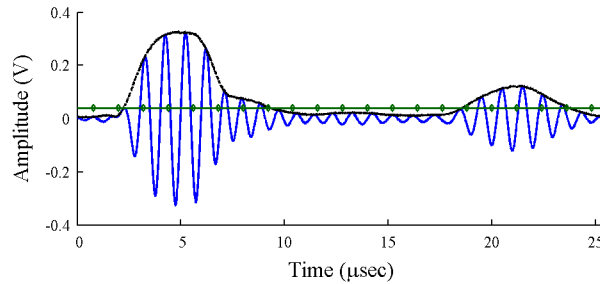


Figure 8: Example for a measured signal (—) with two bursts. The envelope curve (--) is obtained from the procedures based on Hilbert transform. The threshold (—◆—) is used to distinguish signal from noise.

Once the signal burst is identified, only the data samples around the burst need to be transmitted to the server. For example, assuming that both the first and the second tone bursts in figure 8 last about  $8 \mu\text{s}$ , less than 70 samples in total need to be transmitted (with  $f_s = 8.3334 \text{ MHz}$ ). Compared to the number of 4096 samples obtained from every ultrasonic test, the amount of data to be transmitted is reduced to less than 2% of the original data. In addition, if only the peak amplitudes of the two bursts are of interest as damage signatures, the amount of data that needs to be transmitted is reduced to only 2 samples.

#### 4. Ultrasonic measurements and validation of prototype device

For ultrasonic measurements, the wireless prototype device is incorporated with contact transducers coupled with Plexiglas wedges to create Rayleigh waves in steel. Notches of different depths are tested for damage assessment. This section describes the wave generation in the specimen and the experimental validation of the prototype device.

##### 4.1 Wedge transducers for the generation and detection of Rayleigh surface waves

A commercial narrow-band ultrasonic contact transducer (*Panametrics A103*) coupled with a plexiglas wedge (“wedge transducer”) is used to generate Rayleigh surface waves in the steel specimen as shown in figure 9. Rayleigh surface waves are advantageous for a low-power device, because their energy is confined to a small depth below the surface and they suffer less from geometric attenuation compared with bulk waves. Another nominally identical wedge transducer is used for detecting response signals. The transducers are coupled to the wedges with light lubrication oil and mechanically clamped to the wedges as shown in figure 9(b), and the transducer-wedge assemblies are coupled to the specimen using the same couplant. In real world applications, these wedge transducers can be permanently attached to the structure component being monitored. The transmitting transducer launches longitudinal waves into the wedge, which is designed especially for generating Rayleigh surface waves in steel. The wedge angle ( $\phi$ ) is determined according to the Snell’s law

$$\sin \phi = \frac{c_{Lw}}{c_{Rs}} \quad (11)$$

where  $c_{Lw}$  and  $c_{Rs}$  are the longitudinal wave speed in the wedge and the Rayleigh surface wave speed in steel, respectively. These wave speeds are determined from an independent measurement as  $c_{Rs} = 2963 \text{ m/s}$  and  $c_{Lw} = 2750 \text{ m/s}$ , and the wedge angle is  $\phi = 68.1^\circ$ . Note that this wedge method is known to be among the most efficient in generating Rayleigh waves in the target solid material (Viktorov 1967), and the longitudinal wave speed in the wedge material must be lower than the Rayleigh wave speed in steel. Plexiglas is a commercially available material which meets this requirement and has a relatively low material absorption. The leading bottom edge of the wedge is not perpendicular to the bottom surface (see figure 9(b)), which is to reduce spurious acoustic signals that arise from multiple reflections inside the wedges.



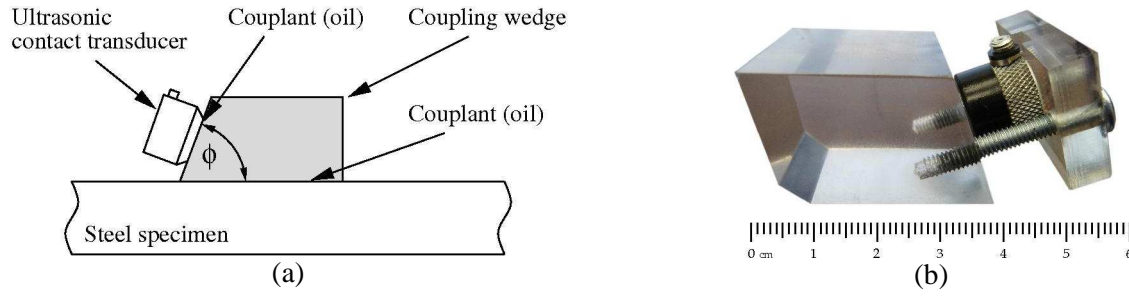


Figure 9. Generation of Rayleigh waves using a wedge transducer: (a) Schematic of the setup; (b) Photo of the wedge transducer

#### 4.2 Test specimen and simulated damage

Thin notches with different depths as simulated surface cracks are cut into a steel plate specimen ( $241 \text{ mm} \times 152 \text{ mm} \times 25.3 \text{ mm}$ ), using an electrical discharge machine (EDM) (figure 10). Table 1 shows the measured dimensions of the notches. Note that the maximum notch opening width is 0.7 mm, simulating a surface fatigue crack that is possibly open by an external load or due to the environmental damage on crack faces (such as corrosion). The thickness of the plate is much larger than the Rayleigh wavelength of 2.9 mm at 1 MHz in steel, which justifies the assumption of the Rayleigh surface wave propagating in an elastic half space. The notches are located sufficiently apart from each other and from the plate boundaries (edges), which allows for a separate examination of each notch without being interfered by scattered signals from other notches or plate boundaries.

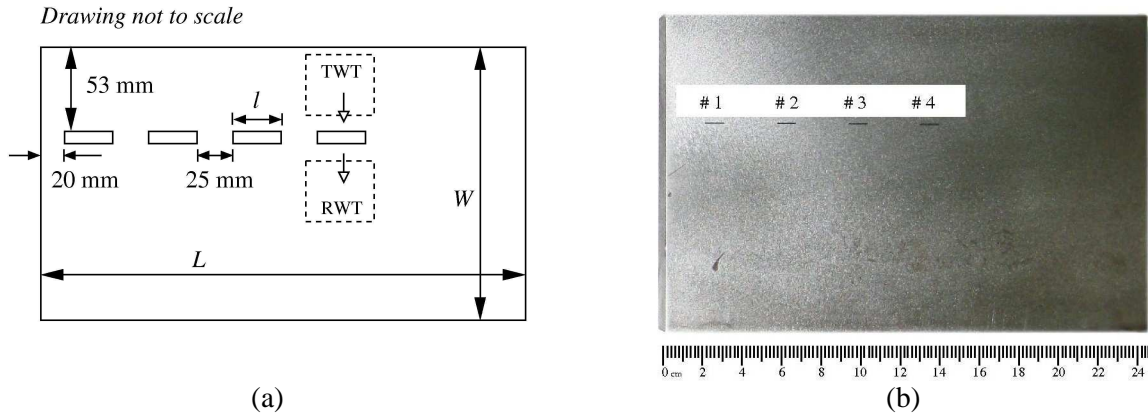


Figure 10. Test specimen with EDM notches: (a) Drawing with example positions of transmitting (TWT) and receiving wedge transducers (RWT); (b) Photo of the specimen. The TWT-RWT configuration in (a) corresponds to notch #4 in (b).

Table 1. Dimensions of the EDM notches in the test specimen

Notch #	Depth* (mm)	Opening Width (mm)	Length** (mm)
1	0.5	0.58	9.3
2	1.2	0.58	9.4
3	2.3	0.63	9.3
4	3.2	0.70	9.3

\* Local maximum depth along the edge of the notch

\*\* Length on the specimen surface.

#### 4.3 Reference ultrasonic measurement

For validating the performance of the prototype wireless device, a reference measurement that employs standard commercial ultrasonic equipment is performed on the steel specimen. The data obtained from the reference measurement are compared to those from the prototype device, in order to verify if the stand-alone prototype device with the power (due to the use of batteries) and memory restrictions can emulate the performance of standard ultrasonic NDE equipment. Two wedge transducers are placed at the front and back of the notch in the pitch-catch setup, so that a forward-scattered ultrasonic signal is detected. Ultrasonic tone burst signals with 5 cycles at 1 MHz are generated with a signal generator (*Agilent 33250A*) and then amplified by a power amplifier (*ENI 325LA RF*) to an output amplitude of  $\pm 15$  V before being fed into the transmitting transducer. This output amplitude is comparable to the amplitude of the  $\pm 18$  V 1-MHz square wave to be generated by the prototype device. On the detection side, the response signals from the receiving transducer are amplified by a pre-amplifier (the receiver of a *Panametrics 5058PR* pulser/receiver is used for this purpose) to the desired amplitude range  $\pm 1.5$  V. This range corresponds to the input range of the analog-digital converter (ADC) of the prototype wireless device. The amplified signal is finally fed into an oscilloscope (*Tektronix TDS 5034* digital storage oscilloscope) which digitizes and saves the acquired signals at a sampling rate of 500 MHz. A Rayleigh wave scattering model for a half-elliptical notch (or crack) may be used to extract the information on the size of the notch (crack) from the received signal (Zhang and Achenbach 1990, Kim and Rokhlin 2002). Inherent to the liquid-coupled contact ultrasonic technique, the variability in the measured amplitude output signals is up to about 10 %. This variability can be greatly reduced by permanently attaching the transducers to the specimen.

Figure 11 shows the ultrasonic signals obtained from the undamaged area of the specimen and from the areas with notches of different depths. As expected, the amplitude of the diffracted wave decreases with the increase of notch depth. In this figure, it is seen that even at the notch depth as small as 0.5 mm, the signal amplitude shows a visible decrease, indicating the sensitivity level of the measurement setup. Note that the diffracted wave signal arrives at the receiver with a small time delay due to the longer path for the wave diffraction at the tip of the notch. In addition to this diffracted wave signal, a second signal appears at around  $47 \mu\text{s}$ ; this signal is absent when there is no notch as shown in figure 11(a). A Rayleigh wave traveling on the

notch surface is mode-converted to a shear wave at the notch (crack) tip (Freund 1971), as illustrated in figure 12. This wave travels down to the plate bottom, where it is reflected back as a shear wave toward the notch tip (Kim and Rokhlin 2002, Rokhlin and Kim 2003). The shear wave is then mode-converted back to a Rayleigh wave. The time of flight for this signal is directly related to the notch depth and the specimen geometry, and therefore, has been successfully used to size small crack depths below 0.3 mm (Kim and Rokhlin 2002, Rokhlin and Kim 2003). The signals after 55  $\mu\text{s}$  are the secondary signals emitted from the wedge due to reflections inside the wedge and other double reflected and mode-converted waves (in the specimen thickness). Since the amplitudes of these signals at later time are small and thus are not practically useful, they are not considered further.

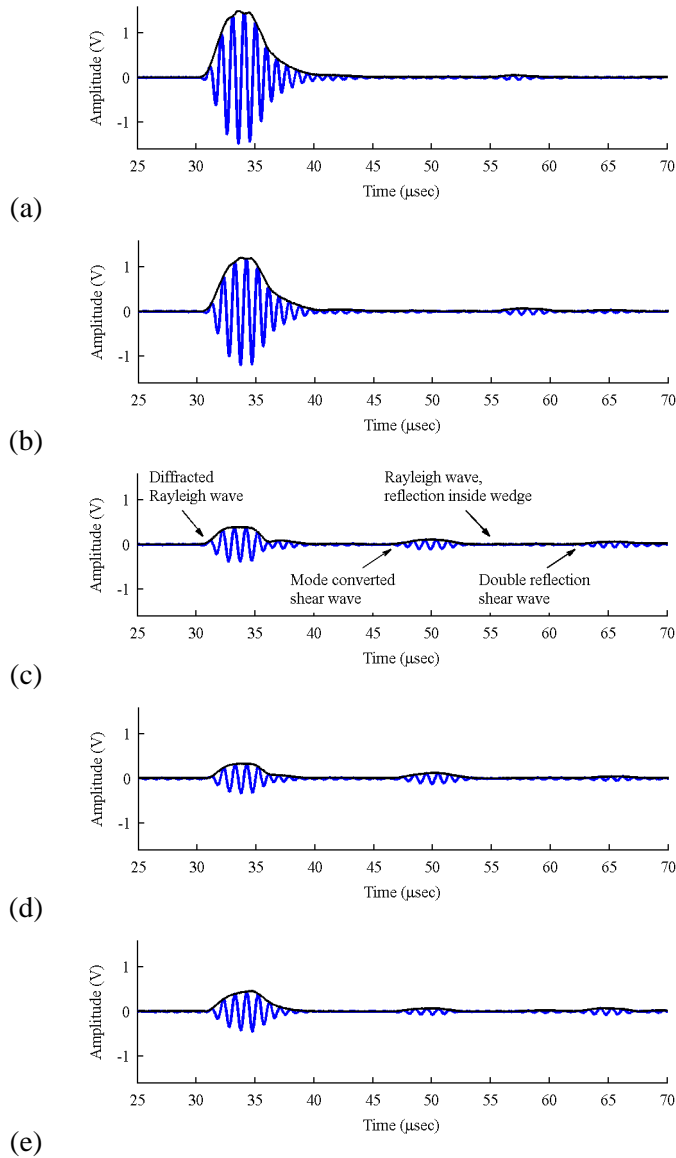


Figure 11. Ultrasonic measurements for different notch depths, taken with commercial ultrasonic equipment, and envelope curves obtained by Hilbert transform: (a) Undamaged specimen; (b) 0.5 mm deep notch; (c) 1.2 mm deep notch; (d) 2.3 mm deep notch; (e) 3.2 mm deep notch. Threshold for the detection of signal bursts: 0.04 V.

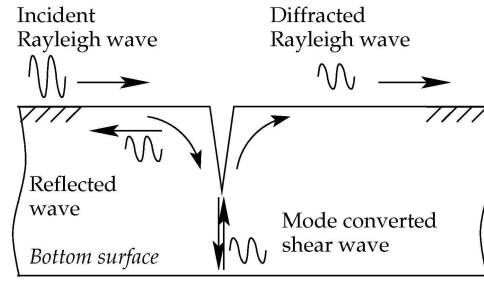


Figure 12. Diffraction and reflection of an incident Rayleigh wave at a crack (side view).

The amplitude transmission coefficient for a notch is defined as

$$T = \frac{V_{\text{env, max}}^{\text{notch}}}{V_{\text{env, max}}^{\text{undamaged}}} \quad (12)$$

where  $V_{\text{env, max}}^{\text{notch}}$  is the peak amplitude of the diffracted wave signal from a notch, obtained from the envelope of this signal, and  $V_{\text{env, max}}^{\text{undamaged}}$  is the peak amplitude of the envelope of the first arrival signal from an undamaged specimen (figure 11(a)). The envelopes of both signals are obtained using the Hilbert transform as described in Section 3.

Table 2. Amplitude transmission coefficients of notches measured by standard NDE equipment

Notch depth	0.5 mm	1.2 mm	2.3 mm	3.2 mm
Transmission Coefficient	0.86	0.37	0.22	0.31

As shown in Table 2, the transmission coefficient decreases as the crack depth increases, because more and more wave energy is reflected. The only outlier is the 3.2 mm deep notch, for which the transmission coefficient is unexpectedly high. The cause of this is yet to be fully investigated. It may be attributed to the fact that the geometry of this 3.2-mm notch can be different from the other notches, and imperfections in the EDM process can lead to a different wave scattering pattern. Nevertheless, the obtained results show a satisfactory level of sensitivity for the ultrasonic monitoring of surface cracks in steel. It is also seen in figure 11 that while the amplitude of the diffracted wave signal decreases, the amplitude of the mode converted shear wave increases with an increasing notch depth. This can provide another parameter useful in estimating the size of the notch or crack, although more detailed ultrasonic data analysis is beyond the scope of this paper.

#### 4.4 Ultrasonic measurement using the prototype wireless device

Ultrasonic measurements are also performed with the prototype device on the same specimen, following the same transducer arrangement as in the reference measurement. The gain and offset of the signal conditioning circuit are adjusted, so that the received signals obtained for an undamaged specimen will occupy nearly the full span of the ADC input range yet without saturation. Figure 13 shows the acquired signals for different notch depths. Clearly, the shapes and the relative amplitudes of the acquired signals are close to those from the reference ultrasonic measurement as shown in figure 11. The same features that correspond to the different propagation paths are well identified from these signals. The signal obtained from the 3.2 mm notch case appears to be opposite of these trends, but is still consistent with the trend in the reference ultrasonic measurement shown in figure 11. These results are both confirmation of the known scattering behavior when the wavelength of the Rayleigh wave is smaller than the notch depth. In this case the scattered field is less sensitive to the notch depth, and much more sensitive to other geometric features of the notch, such as the width around the root (Hirao and Fukuoka 1982). Imperfections in the EDM process probably caused a slightly different geometry of this 3.2-mm notch (compared with the other notches), which contributed to a different wave scattering pattern.

The transmission coefficients for the notches with different depths measured by the prototype device are also listed in table 3. The maximum deviation from those of the reference measurement in table 2 is close to 10%. This deviation is comparable to the variability level of the liquid-coupled contact technique itself, which is also about 10%. This illustrates that the prototype wireless ultrasonic device can provide comparable performance as the standard NDE equipment and thus can be used in monitoring fatigue cracks growing on the surface of a similar material.

*Table 3. Amplitude transmission coefficients of notches measured by the prototype wireless device*

Notch depth	0.5 mm	1.2 mm	2.3 mm	3.2 mm
Transmission Coefficient	0.94	0.36	0.21	0.29
Deviation from Table 2 (%)	-9.3	2.7	4.5	6.5

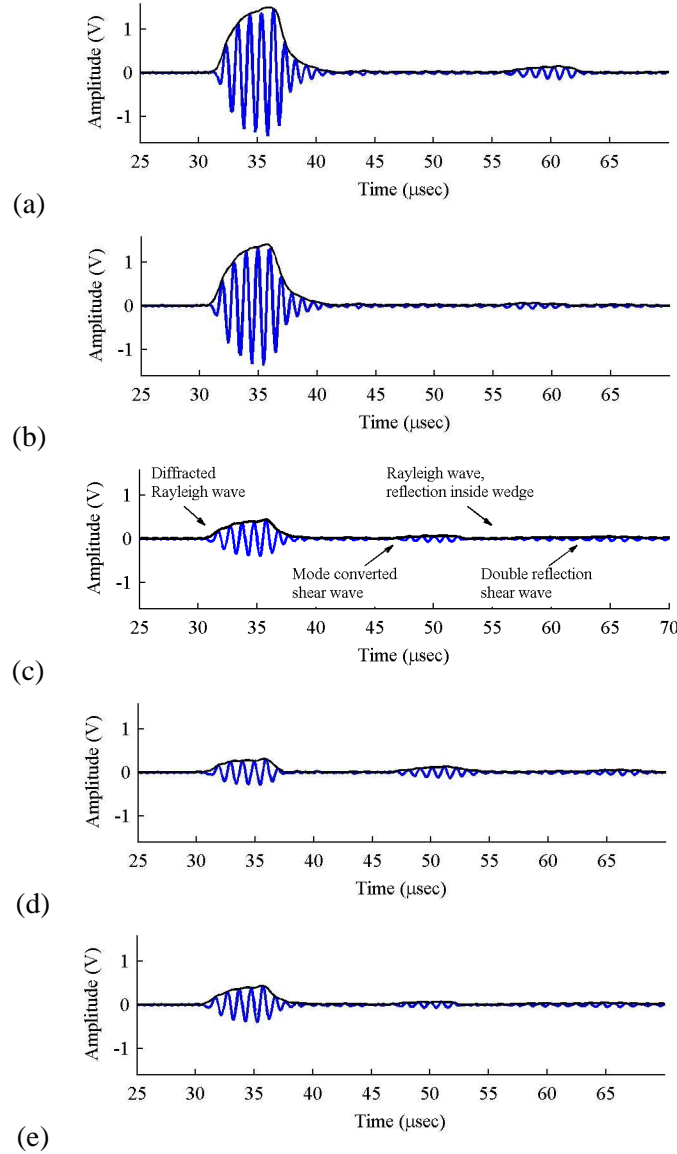


Figure 13. Ultrasonic measurements for different notch depths, taken with the prototype wireless device, and envelope curves obtained by Hilbert transform: (a) Undamaged specimen; (b) 0.5 mm deep notch; (c) 1.2 mm deep notch; (d) 2.3 mm deep notch; (e) 3.2 mm deep notch. Threshold for detection of signal bursts: 0.04 V.

## 5. Summary and discussion

This study examines the feasibility of continuous ultrasonic monitoring using a compact, battery-powered, and self-contained device. The prototype device has been designed, implemented, and tested, using Rayleigh waves with a center frequency of around 1 MHz. Powered by small-size batteries, the stand-alone device can generate an 18 V tone burst signal for ultrasonic excitation, as well as provide a high sampling rate of 8.3334 MHz for measuring response signals. The contact wedge mechanism for Rayleigh wave generation proves to be efficient, which enables ultrasonic measurements with the limited excitation voltages provided by battery power. Experimental results illustrate the performance of the prototype device is reasonably close

to the performance of standard commercial ultrasonic equipment, in terms of detecting mm-size notches on a steel specimen.

For future field deployment, small solar panels will be sufficient in harvesting enough energy for the recharging the batteries of the device, or vibration energy harvesters may be explored. The device operation can be controlled by a remote server through wireless communication, which eliminates the time and monetary cost for running long cables on the structure. Future development can also emphasize more on reducing the device size, and explore the performance of arrays of such devices for more accurate damage detection. Last but not least, in the current study, only a phenomenological analysis of the ultrasonic signals has been performed. Detailed quantitative analyses and more extensive tests of the device are subjects of future work.

### Acknowledgements

The authors appreciate the financial support for first author provided by the German Academic Exchange Service (DAAD). This research is partially funded by the National Science Foundation under Grant Number CMMI-0928095, awarded to Prof. Yang Wang. The authors would like to thank Kyle M. French of the electronics lab at The George W. Woodruff School of Mechanical Engineering at Georgia Tech, for his assistance with designing the output amplification and signal conditioning circuits.

### References

- Bedrosian E 1963 A Product Theorem for Hilbert Transforms *Proceedings of the IEEE* **51** pp 868–9
- Çelebi M 2002 Seismic Instrumentation of Buildings (with Emphasis on Federal Buildings) *USGS Project no.: 0-7460-68170*, United States Geological Survey (MS977) Menlo Park, CA, USA
- Chang P C; Flatau A and Liu S C 2003 Review Paper: Health Monitoring of Civil Infrastructure *Structural Health Monitoring* **2** 257–67
- Digi International Inc. 2010 *Application note – 900 MHz vs 2.4 GHz*.  
<http://www.digi.com/support/kbase/kbaseresultdetl.jsp?kb=64>. Last accessed: 09/10/2010.
- Elgamal A, Conte J P, Masri S, Fraser M, Fountain T, Gupta A, Trivedi M and El Zarki M 2003 Health monitoring framework for bridges and civil infrastructure *Structural Health Monitoring 2003* pp 123–30
- Freund L B 1971 The oblique reflection of a Rayleigh wave from a crack tip *Int J Solids Struct* **7** 1199–1210
- Grisso B L, Martin L A and Inman D J 2005 A wireless active sensing system for impedance-based structural health monitoring. *Proc. of the 23rd International Modal Analysis Conference (IMAC XXIII)*, (Orlando, FL)
- Hahn S L 1996 *Hilbert Transform in Signal Processing*, Artech House
- Hirao M and Fukuoka H 1982 Scattering of Rayleigh surface waves by edge cracks: Numerical simulation and experiment *J. Acoust. Soc. Am.* **72** 602–6

Horowitz P and Hill W 1989 *The Art of Electronics*, Cambridge University Press, New York, NY, USA

Johnson D & Associates 2000 300V Peak to Peak Signal Generator <http://www.discovercircuits.com/PDF-FILES/300vpp.pdf>, Last accessed: 08/16/2009.

Kim J-Y and Rokhlin S I 2002 Surface acoustic wave measurements of small fatigue cracks initiated from a surface cavity *Int. J. Solids Struct.* **39** 1487–1504

Kim S, Pakzad S, Culler D, Demmel J, Fenves G, Glaser S and Turon M 2007 Health monitoring of civil infrastructures using wireless sensor networks. *Proc. of the 6th International Conference on Information Processing in Sensor Networks (IPSN '07)* (Cambridge, MA) pp 254-63

Liu L and Yuan F G 2008 Active damage localization for plate-like structures using wireless sensors and a distributed algorithm *Smart Materials and Structures* **17** 055022

Lynch J P 2005 Design of a wireless active sensing unit for localized structural health monitoring *Structural Control and Health Monitoring* **12** 405-23

Lynch J, Wang Y, Loh K, Yi J-H and Yun C-B 2006 Performance Monitoring of the Geumdang Bridge Using a Dense Network of High-Resolution Wireless Sensors *Smart Materials and Structures* **15**(6) 1561–75

Lyons R G 2004 *Understanding Digital Signal Processing 2<sup>nd</sup> ed*, Prentice Hall, Englewood Cliffs, NJ

Marple S L Jr 1999 Computing the Discrete-Time ‘Analytic’ Signal via FFT', *IEEE Trans. Signal Process* **47**(9) 2600–3

Mascarenas D L, Todd M D, Park G and Farrar C R 2007 Development of an impedance-based wireless sensor node for structural health monitoring *Smart Materials and Structures* **16** 2137-45

Meyendorf N, Rokhlin S I and Nagy P B (Ed.) 2004 *Nondestructive Materials Characterization: with Applications to Aerospace Materials* Springer, New York.

Moore M, Phares, B, Graybeal, B, Rolander, D and Washer G June 2001 *Reliability of visual inspection for highway bridges, vol. I: Final report*. Technical Report FHWA-RD-01-020, (U.S. Department of Transportation, Federal Highway Administration)

Nagayama T and Spencer B F, Jr. 2007 *Structural Health Monitoring using Smart Sensors*. (Urbana, IL: Newmark Structural Engineering Laboratory, University of Illinois at Urbana-Champaign)

Park S, Yun C-B and Inman D J 2006 Wireless structural health monitoring using an active sensing node *Int. J. Steel. Struct.* **6** 361-8

Pertsch A T, Kim J-Y, Wang Y and Jacobs L J 2009 An intelligent stand-alone ultrasonic device for monitoring local damage growth in civil structures *Proc. 36th Annual Review of Progress in Quantitative Nondestructive Evaluation*

Press W H, Teukolsky S A, Vetterling W T and Flannery B P 1992 *Numerical Recipes in C (2nd ed.)*: *The Art of Scientific Computing*, Cambridge University Press, New York, NY, USA.

Resch M T and Nelson D V 1992 An ultrasonic method for measurement of size and opening behavior of surface fatigue cracks *Small-crack test methods*, ASTM STP 1149, Edited by Larsen J M and Allison J E, 169~196.



Rokhlin S I and Kim J-Y 2003 In-situ ultrasonic monitoring of surface fatigue crack initiation and growth from a surface cavity *Int. J. Fatigue* **25** 41–49

Sohn H, Farrar C R, Hunter N F, and Worden K 2001 Structural health monitoring using statistical pattern recognition techniques *J. Dynamic Systems, Measurement, and Control* **123** 706–11

Straser E G and Kiremidjian A S 1998 A Modular, Wireless Damage Monitoring System for Structures *Report No. 128, John A. Blume Earthquake Engineering Center, Department of Civil and Environmental Engineering* Stanford University, Stanford, CA.

Tien J J W, Khuri-Yakub B T, Kino G S, Marshall D B and Evans A G 1981 Surface acoustic wave measurement of surface cracks in ceramics *J Nondestruct Eval* **2**(3,4) 219~229.

U.S. Department of Transportation, Federal Highway Administration 2009a *Deficient bridges by state and highway system as of december 2008* <http://www.fhwa.dot.gov/Bridge/nbi/defbr08.cfm>, Last accessed: 09/10/2010.

U.S. Department of Transportation, Federal Highway Administration 2009b *FHWA bridge programs structure type by year built*. <http://www.fhwa.dot.gov/Bridge/structyr.cfm>, Last accessed: 09/10/2010.

Viktorov I A 1967 *Rayleigh and Lamb Waves – Physical Theory and Applications* (New York: Plenum Press).

Wang Y, Lynch J P and Law K H 2007 A Wireless Structural Health Monitoring System with Multithreaded Sensing Devices: Design and Validation *Structure and Infrastructure Engineering* **3**(2) 103–20

Wang Y, Loh K, Lynch J, Fraser M, Law K and Elgamal A 2006 Vibration Monitoring of the Voigt Bridge Using Wired and Wireless Monitoring Systems *Proc. 4th China-Japan-US Symposium on Structural Control and Monitoring*

Weng J-H, Loh C-H, Lynch J P, Lu K-C, Lin P-Y and Wang Y 2008 Output-only modal identification of a cable-stayed bridge using wireless monitoring systems *Engineering Structures* **30** 1820-30

Zhang C and Achenbach J D 1990 Dispersion and attenuation of surface waves due to distributed surface-breaking cracks *J. Acoust. Soc. Am.* **88** 1986–92